

Droplet Microfluidics for the Label-Free Extraction of Complete Phase Diagrams and Kinetics of Liquid–Liquid Phase Separation in Finite Volumes

Alessia Villois, Umberto Capasso Palmiero, Prerit Mathur, Gaia Perone, Timo Schneider, Lunna Li, Matteo Salvalaglio,* Andrew deMello,* Stavros Stavrakis,* and Paolo Arosio*

Liquid–liquid phase separation of polymer and protein solutions is central in many areas of biology and material sciences. Here, an experimental and theoretical framework is provided to investigate the thermodynamics and kinetics of liquid–liquid phase separation in volumes comparable to cells. The strategy leverages droplet microfluidics to accurately measure the volume of the dense phase generated by liquid–liquid phase separation of solutions confined in micro-sized compartments. It is shown that the measurement of the volume fraction of the dense phase at different temperatures allows the evaluation of the binodal lines that determine the coexistence region of the two phases in the temperature-concentration phase diagram. By applying a thermodynamic model of phase separation in finite volumes, it is further shown that the platform can predict and validate kinetic barriers associated with the formation of a dense droplet in a parent dilute phase, therefore connecting thermodynamics and kinetics of liquid–liquid phase separation.

including thermoresponsive smart materials,^[1–4] cellular compartmentalization,^[5,6] origin of life,^[7–10] and synthetic biology.^[11,12] In all these contexts, phase diagrams contain crucial information about the intermolecular forces driving the process as well as the effect of modulators on phase separation.^[13] Such phase diagrams typically report the concentration of a macromolecule in the dilute and dense phase as a function of temperature or other modulators of intermolecular interactions, such as ionic strength or pH (Figure 1A).

A variety of experimental techniques have been developed to measure the saturation concentration, i.e., the critical polymer concentration above which phase separation occurs. These methods include optical microscopy, turbidimetry, and light scattering.^[14] Typically, the cloud-point

1. Introduction

Liquid–liquid phase separation of polymer and protein solutions plays an important role in a variety of research fields,


temperature (T_{cp}) is evaluated by varying temperatures at one fixed polymer concentration or, alternatively, the saturation concentration is estimated by progressively increasing the polymer concentration at constant temperature (Figure 1A). Recent techniques based on droplet-based microfluidics^[15–21] and Taylor dispersion analysis^[22] enable these measurements to be performed at high-throughput. These methods have been successfully applied to evaluate the left arm of the binodal, which is the coexistence curve that defines the two-phase region (Figure 1A).

In contrast, the measurement of the concentration of polymers inside the dense phase (the right arm of the binodal) is more challenging, since it typically requires a large amount of material. Important studies have reported complete phase diagrams of lens proteins, lysozyme, and albumin.^[23–27] However, in general, measurements of the complete phase diagram are less common than saturation concentrations. Yet, this information is crucial since the concentration in the dense phase is related to important material properties, such as water content, permeability, and viscoelasticity.^[28]

Recently, phase separation has attracted enormous interest in biology in association with a class of membraneless organelles formed by phase separation of proteins and nucleic acids.^[29,30] The measurement of the full phase diagrams of this class of molecule is even more challenging due to the relatively small amount of material that is typically available for

A. Villois, U. Capasso Palmiero, P. Mathur, G. Perone, T. Schneider, A. deMello, S. Stavrakis, P. Arosio
Department of Chemistry and Applied Biosciences
Institute for Chemical and Bioengineering
ETH Zurich
Zurich 8093, Switzerland
E-mail: andrew.demello@chem.ethz.ch; stavros.stavrakis@chem.ethz.ch; paolo.arosio@chem.ethz.ch

L. Li, M. Salvalaglio
Thomas Young Centre and Department of Chemical Engineering
University College London
London WC1E 7JE, UK
E-mail: m.salvalaglio@ucl.ac.uk

 The ORCID identification number(s) for the author(s) of this article can be found under <https://doi.org/10.1002/smll.202202606>.

© 2022 The Authors. Small published by Wiley-VCH GmbH. This is an open access article under the terms of the Creative Commons Attribution-NonCommercial-NoDerivs License, which permits use and distribution in any medium, provided the original work is properly cited, the use is non-commercial and no modifications or adaptations are made.

DOI: 10.1002/smll.202202606

analysis. Unsurprisingly, complete phase diagrams of phase separating proteins are still limited in the literature. Notable examples however include the phase diagram of regions of the proteins Ddx4,^[31] Laf1,^[28] and hnRNAP1^[32,33] evaluated by fluorescence correlation spectroscopy (FCS) or turbidimetry, as well as concentration in the dense phase assessed by Raman spectroscopy^[34] or by label-free quantitative phase microscopy.^[35]

Herein, we develop an alternative approach for the extraction of complete phase diagrams, which is based on droplet-based microfluidics and requires a few hundreds of microliters of unlabeled sample. The core of the strategy involves the accurate measurement of the volume of the dense phase when the phase separating solution is confined in water-in-oil compartments.^[15,36] From the volume of the dense phase, the concentration of the scaffold molecules in the dilute and dense phase can be calculated from the law of mass conservation, under the assumption that the concentration in the dense and dilute phase are independent of the initial polymer concentration in the investigated range.

In the first part of this paper, we coupled this approach with on-chip temperature control to measure the saturation concentration and the concentration in the dense phase at different temperatures, therefore estimating the full temperature-concentration phase diagram.

In the second part of the work, we applied a thermodynamic model of phase separation in finite volumes (nL) to predict nucleation barriers for droplet formation, which we then validated with a second microfluidic platform designed to monitor kinetics of phase separation. Significantly, we could estimate the time scale for phase separation as a function of supersaturation, even in the case of a non-activated system dominated by diffusion. Overall, this framework provides a connection between the thermodynamics and kinetics of phase separation.

We used our method to analyze the associative coacervation of two synthetic polymers that mimic the behavior of biologically relevant intrinsically disordered proteins.^[37] In particular, we characterized a zwitterionic polymer that exhibits upper critical solution temperature (UCST)-type behavior of many low complexity domains^[38,39] and a poly(ethylene glycol)-based polymer that resembles the low critical solution temperature (LCST)-type behavior of many elastin-like peptides (ELPs)^[39–41] (see structures in Figure S1, Supporting Information). The UCST zwitterionic polymer is composed of the monomers sulfobetaine methacrylate (SB) and sulfobetaine methacrylate (ZB) (Figure S1, Supporting Information). In addition to mimicking biological proteins, we selected this responsive UCST zwitterionic polymer since we have recently demonstrated that it holds great promise for several applications in bioengineering, including detection of analytes in droplet microfluidic format.^[37] Understanding the dynamics and thermodynamics of the phase separation of this polymer in confined compartments is therefore attractive from both a fundamental and practical point of view. Moreover, we validated the technique also with an engineered protein based on the adenylate kinase enzyme (AK) conjugated with intrinsically disordered domains taken from the protein Laf1.^[34,42] The phase separation behavior of this protein has been previously characterized in bulk in our laboratory.^[34,42]

2. Summary of Device Fabrication and Operation

Microfluidic structures were fabricated using standard soft-lithographic techniques^[43] (see Figures S2–S6, Supporting Information for detailed description). Two types of droplet-based microfluidic devices were developed: the first one allows trapping of droplets and long-term monitoring of their content at different temperatures, therefore enabling the generation of phase diagrams according to the principle described in this paper. The second device allows examination of droplet content in flow, and was applied to analyze the kinetics of liquid–liquid phase separation (LLPS) at different temperatures. Both devices incorporate a transparent indium tin oxide coating to achieve a homogenous heating through the Joule effect (Figure 1B). During all experiments, the temperature was monitored with a thermocouple placed at the bottom of the heating zone.

Water-in-oil droplets were generated in a flow focusing geometry and trapped only after droplet generation was stabilized. To achieve such conditions, fluorinated HFE-7500 oil containing 0.5% v/v surfactant was introduced at 3 $\mu\text{L min}^{-1}$ via the device outlet (Figure 1B), while droplets were simultaneously generated at the device inlets. Due to the back pressure of the oil from the outlet, the first generated droplets were prevented from entering the trap array and left the device via the secondary outlet. Once the droplet generation was stabilized, the back-oil flow was stopped to allow droplets entering the trap array. This configuration ensures that only droplets generated at steady state can be stored in the traps.

3. Complete Phase Diagrams of Liquid–Liquid Phase Separation at Finite Volumes

Figure 1B shows a schematic representation of the droplet microfluidic device, which comprises three regions: in the first area the polymer solution (reagent 1) is diluted with a “trigger” of liquid–liquid phase separation (reagent 2), and the mixture is then compartmentalized in water-in-oil droplets. In this context we define as trigger a modulator of the solution conditions that changes the saturation concentration and promotes LLPS. Typically, phase separation can be triggered by mixing the sample with a solution at different ionic strength or pH value, or by introducing molecules which can act as seeds. In the case of the UCST polymer, phase separation was promoted by diluting the stock of a homogeneous sample at high salt concentration with pure water. The decrease of salt concentration strengthens the intermolecular electrostatic attractive interactions that compensate the entropic cost of the demixing and induce phase separation.^[37] In the case of the LCST polymer, the trigger responsible for phase separation was the increase of temperature in the heating zone and no changes in the composition of the stock solution were required. In this case, phase separation is entropy-driven: the solution is homogeneous at room temperature and spontaneously phase-separates at high temperature.

In the second region of the device, droplets travel through a winding channel with chaotic advection promoting intensive mixing in their interior, and guaranteeing homogeneous conditions within milliseconds.^[44] After mixing is complete, droplets

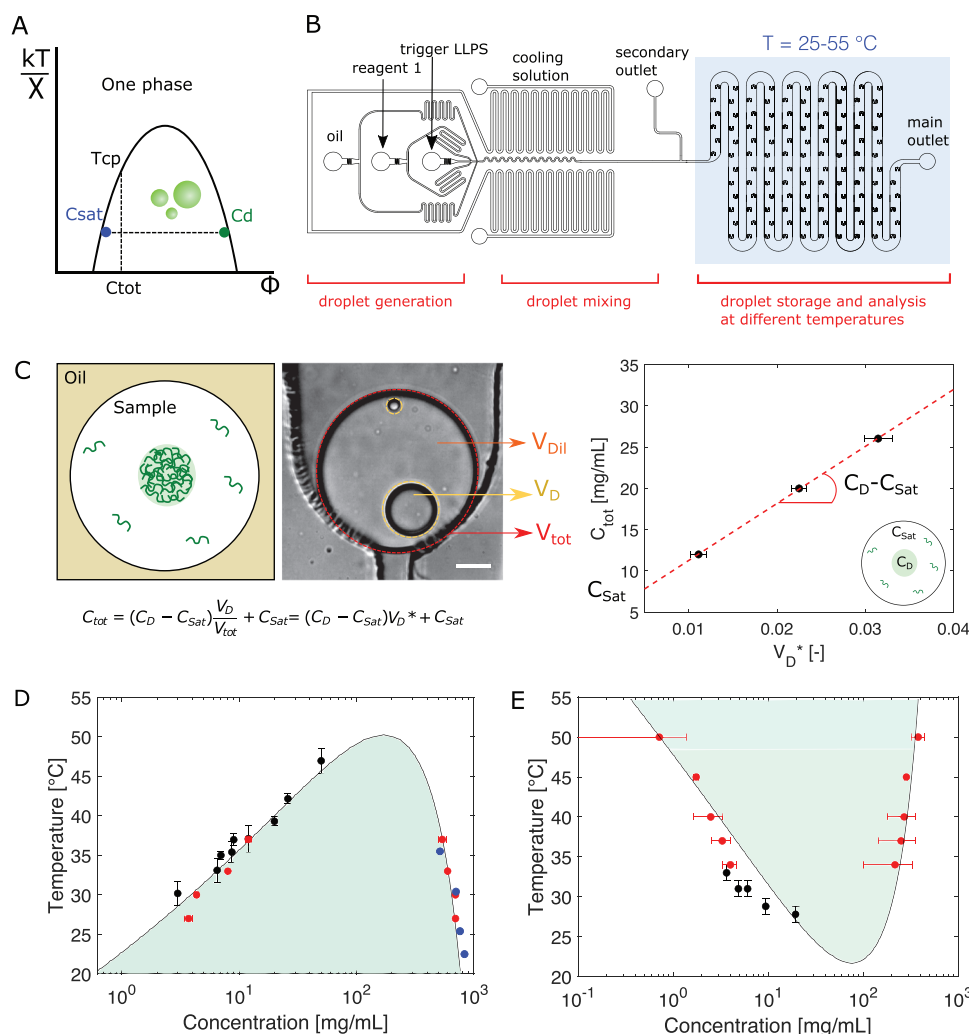


Figure 1. A) Binodal curves define the coexistence region of the two phases in the temperature versus polymer concentration (Φ) phase diagram. T_{cp} = cloud point temperature; C_{sat} = saturation concentration, i.e., the concentration in the dilute phase when phase separation occurs; C_d = concentration in the dense phase; C_{tot} = total concentration of polymer introduced in the solution. On the y axis temperature is normalized by the interaction parameter (X). B) Schematic representation of the droplet-based microfluidic device. The blue background indicates the heating zone; C) (left) Schematic and representative brightfield image of an individual water-in-oil compartment in which LLPS is observed from a 20 g L^{-1} polymer solution. From image analysis, the total volume of the external compartment (V_{tot}) as well as the volume of the dense (V_D) and dilute phase (V_{Dil}) are measured. Scale bar corresponds to $20\text{ }\mu\text{m}$. (right) Representative plot of the initial concentration of the polymer as a function of the measured normalized total volume of the dense phase (V_D^*). The red dotted line represents the linear fit according to the mass balance, from which the concentration of polymer in the dilute and dense phase can be estimated. Error bars represent standard deviations estimated from at least five independent water-in-oil droplets. D–E) Phase diagrams of D) UCST-type polymer (based on poly(sulfobetaine-*co*-sulfobetaine methacrylates), 70SB-130ZB,^[37] see Figure S1, Supporting Information) in 150 mM NaCl solution and of E) LCST-type polymer (based on poly(oligoethylene glycol methacrylates) 36EG₂MA-4EG₄MA, see Figure S1, Supporting Information) in ultra-pure water. The red symbols represent concentrations measured with the method described in this work. Black and blue circles represent orthogonal measurements based on microscopy and fluorescence correlation spectroscopy, respectively.

enter the third zone, in which temperature is controlled by a power generator connected to the ITO-coated glass by an electrical circuit. In this area, traps having a “C”-shape are structured inside the channels. These traps act to block individual droplets, as previously reported,^[45] and allow their imaging by brightfield microscopy at different temperatures.

For each individual compartment, the volume of the water-in-oil compartment (V_{tot}), the total volume of the dense phase (V_D), and the total volume of dilute phase (V_{Dil}) were calculated by image analysis (Figure 1C and Figure S7, Supporting

Information). The normalized dense phase volume (V_D^*) was evaluated as the ratio between the total volume of the dense phase (V_D) and the volume of the water-in-oil compartment (V_{tot}).

For each condition, this experiment was repeated at different initial concentrations of the polymer inside the water-in-oil compartment (C_{tot}) between 1 and 30 mg mL^{-1} (see representative example in Figure 1D). From the measured volumes and the law of mass conservation:

$$C_{tot} = (C_D - C_{Sat}) V_D^* + C_{Sat} \quad (1)$$

The concentration of polymer in the dilute phase (C_{Sat}) and dense phase (C_{D}) were estimated from a linear fitting of the experimental data (Figure 1C). We repeated the experiment at different temperatures to evaluate the full phase diagrams of the two polymers (Figure 1D,E). For the UCST polymer at 27 °C we measured a volume fraction of the dense phase between 1.2% and 3.2%, depending on the initial polymer concentration. From Equation (1) we evaluated the concentration of polymer in the dense phase equal to $696 \pm 12 \text{ g L}^{-1}$ at 27 °C (Figure 1D). This value was validated by independently measuring the water content and the density of the dense phase via gravimetry (see Supporting Information).^[37] The measured weight water fraction ($53 \pm 2 \text{ wt\%}$) and density of the dense phase ($1230 \pm 50 \text{ g L}^{-1}$) correspond to a polymer concentration in the dense phase of $\approx 580 \text{ g L}^{-1}$. This value is consistent with the measured concentration of 696 g L^{-1} .

The right arm of the binodal in Figure 1D was further validated by FCS (see Figure S8 and Supporting Information), which provided polymer concentrations in the droplets consistent with the values measured microfluidically.

Finally, to validate the left arm of the measured binodal, cloud point temperatures were measured by progressively heating the water-in-oil compartments at constant polymer concentrations. The disappearance and formation of polymer-rich droplets were observed by optical microscopy. The cloud point temperatures obtained from this set of experiments (black circles in Figure 1D,E) were consistent with the values measured using the microfluidic approach. Moreover, the experimental data were consistent with a Flory–Huggins model, as shown by the fitted simulations in Figure 1D,E (see also Supporting Information).

In the case of the LCST polymer, the dense droplets were smaller and their quantification was associated to a larger error, leading to larger variation in the measured concentrations in Figure 1E.

The microfluidic assay was further validated with an engineered protein based on the adenylate kinase enzyme (AK) conjugated with intrinsically disordered domains taken from the protein Laf1.^[34,42] Also in this case, the measured concentration in the dense phase was in well agreement with the value obtained by FCS (Figure S9, Supporting Information).

The phase separation differential which can be measured with the droplet microfluidic method depends on the initial concentration of the macromolecule and the smallest volume fraction of the dense phase that can be detected with the applied set-up (for our system $\approx 0.25\%$).

While our polymer has negligible solubility in the continuous oil phase, we note that applications of this method to other systems should check for possible release of the solute from the water compartments to the surrounding oil phase.

4. Activation Energies and Kinetics of Liquid–Liquid Phase Separation at Finite Volumes

In addition to the complete phase diagram, the estimation of the volume fraction of the dense phase in finite volumes (nL) (Figure 1C) opens up the possibility of evaluating the kinetic barrier associated with the nucleation and growth of droplets.

A series of recent works have shown that the nucleation rate of liquid–liquid phase separation follows the Classical Nucleation Theory, at least on the mesoscale.^[46–49] We calculated the free energy (reversible work) of formation of a dense liquid droplet of volume V_{D}^* in a finite volume V_{tot} as a combination of two terms (see Supporting Information for a detailed derivation). The first term takes into account the excess free energy difference associated with the phase transition between the dilute and dense phase. The second term describes the excess free energy penalty associated with the formation of an interface between the dense and dilute phases, which is proportional to the surface per unit volume of the dense liquid droplet via a surface tension term, σ . Accordingly, the (adimensional) reversible work (F') takes the form:

$$F' = \frac{M_{\text{p}} F}{\rho^{\text{L}} V_{\text{tot}} RT} \sim -V_{\text{D}}^* \left[\ln \frac{c_{\text{tot}} - \rho^{\text{L}} V_{\text{D}}^*}{c^{\text{L},*} (1 - V_{\text{D}}^*)} + \frac{\Delta \mu^{\text{E}}}{RT} \right] + \sigma' (3V_{\text{D}}^*)^{2/3} \left(\frac{4\pi}{V_{\text{tot}}} \right)^{1/3} \quad (2)$$

where M_{p} is the molar mass of the polymer, ρ^{L} is the polymer concentration in the dense phase, and σ' is the normalized surface tension of the dense liquid ($\sigma' = \sigma M_{\text{p}} / \rho^{\text{L}} RT$).

The measurements shown in the previous paragraph allowed us to estimate the difference in excess chemical potential associated with the transition of a polymer chain from the dilute to dense phase ($-\Delta \mu^{\text{E}}/RT$). Indeed, the reversible work F' is a non-monotonic function of the droplet size that exhibits at least one stationary point corresponding to the equilibrium for a droplet of dense liquid immersed in a dilute parent phase, which can be identified as the local minimum of the reversible work of droplet formation as a function of V_{D}^* (Figure 2A). In some cases,^[50–52] a second stationary point at lower V_{D}^* is present, representing the volume of the critical nucleus associated with the nucleation of the dense liquid phase (Figure 2A). At steady state conditions, the mean thermodynamic force acting on the dense phase droplet is null. This condition corresponds to a stationary point $V_{\text{D}}^{*,\text{SS}}$ in the free energy curve, where $dF/dV_{\text{D}}^* = 0$:

$$\frac{dF}{dV_{\text{D}}^*} = -\ln \left[\frac{c_{\text{tot}} - \rho^{\text{L}} V_{\text{D}}^{*,\text{SS}}}{c^{\text{L},*} (1 - V_{\text{D}}^{*,\text{SS}})} \right] - \frac{\Delta \mu^{\text{E}}}{RT} + \frac{V_{\text{D}}^{*,\text{SS}} (\rho^{\text{L}} - c_{\text{tot}})}{(V_{\text{D}}^{*,\text{SS}} - 1)(\rho^{\text{L}} V_{\text{D}}^{*,\text{SS}} - c_{\text{tot}})} + \frac{2\sigma' (4\pi/V_{\text{tot}})^{1/3}}{(3V_{\text{D}}^{*,\text{SS}})^{1/3}} = 0 \quad (3)$$

From the measurements shown in Figure 1 we evaluated the steady-state volume fraction of the droplet ($V_{\text{D}}^{*,\text{SS}}$), the critical concentration ($c^{\text{L},*}$), and the concentration of the polymer in the dense phase (ρ^{L}) at different temperatures. The parameters c_{tot} and V_{tot} are known inputs of the experimental setup and the effective surface tension of the dense liquid droplets (σ') can be estimated from characteristic values reported in the literature for polymer coacervates.^[6,53] From a global fit of Equation (3) at different temperatures, we estimated the unknown excess chemical potential ($-\Delta \mu^{\text{E}}/RT$), which in turn allowed us to estimate the energy (F) as a function of the droplet volume via Equation (2) (Figure 2B). The calculated energies show a single minimum and the absence of a critical nucleus (Figure 2B),

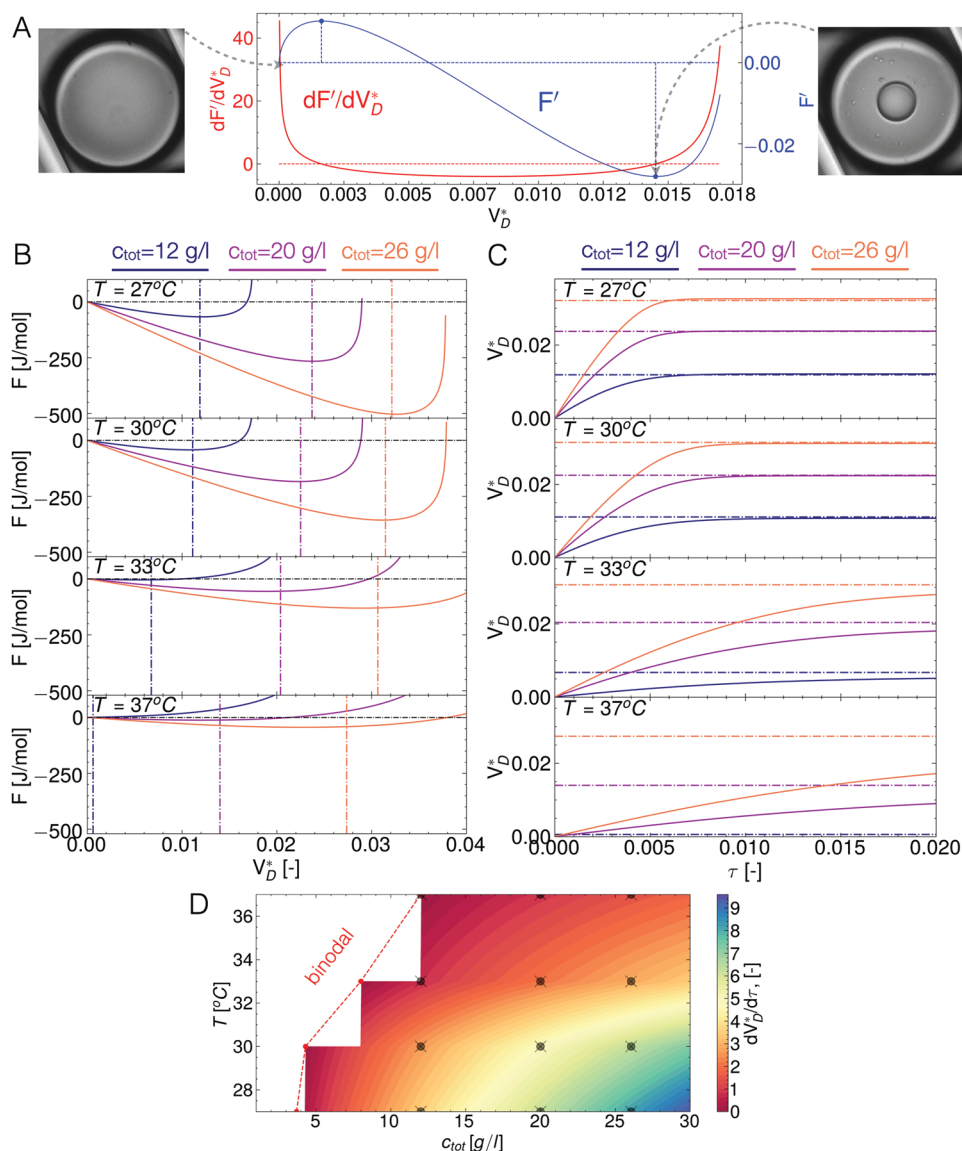


Figure 2. A) Representative plot of the adimensional free energy of nucleation of a dense liquid droplet (F' , blue line) as a function of the droplet size. The non-monotonic function admits at least one stationary point, corresponding to the equilibrium for a droplet of dense liquid immersed in a dilute parent phase. The red line indicates the derivative of the free energy as a function of the droplet volume. Dot lines visualize null values. Images are shown for illustration purpose only; B) The work (F) as a function of the droplet size at different temperatures and at different initial polymer concentrations (blue: 12 g L⁻¹; violet: 20 g L⁻¹; yellow: 26 g L⁻¹). Vertical dashed lines indicate experimental values of steady-state V_D^* . C) Changes of V_D^* as a function of the adimensional time $\tau = tD$ (see Equation (4)) for different regions in the phase diagram. The horizontal dashed lines represent the experimentally measured steady-state V_D^* . D) The kinetics of droplet formation (represented by $dV_D^*/d\tau$) decrease moving toward the binodal line, together with a decrease in supersaturation ($c_{tot}/c^{l,*}$).

indicating that the process is not activated in the range of conditions analysed in this work. Our model predicts that the kinetic barrier for droplet formation is essentially negligible.

Under these conditions, the evolution of a dense liquid droplet is dominated by the growth of a post-critical droplet, which under the typical assumption of overdamped Langevin dynamics,^[54,55] can be captured by the expression:

$$\frac{dV_D^*}{dt} = -D \frac{dF'}{dV_D^*} \quad (4)$$

Here dF'/dV_D^* is the adimensional thermodynamic force associated with the nucleation of a droplet of reduced volume V_D^* (Figure 2B), and D is a diffusion coefficient in reaction coordinate space. Assuming D to be independent of V_D^* and constant across all conditions, we simulated the changes of V_D^* as a function of an adimensional time $\tau = tD$ for different regions in the phase diagram (Figure 2C). The kinetics of droplet formation (represented by $dV_D^*/d\tau$) decrease toward the binodal line (Figure 2D), together with a decrease in supersaturation ($c_{tot}/c^{l,*}$).

To verify the absence of significant kinetic barriers, we modified our microfluidic device to monitor the kinetics of formation of polymer-rich droplets at different temperatures. In this configuration, the C-traps were removed and droplets were allowed to travel along the channel (Figure 3A). Brightfield images were acquired at different locations along the channel, corresponding to different residence times between 3 and 12 s. From the extracted images, the changes in the size distribution of the population of polymer-rich droplets were analysed over time (Figure 3B,C).

Experiments were performed at different values of supersaturation of the UCST polymer, which were obtained by changing either the initial polymer concentration (1.5 and 6.7 mg mL⁻¹) at 24 °C, or temperature values (24 and 32 °C)

at constant polymer concentration (Figure 3D). In agreement with model predictions, we observed that conditions that are closer to the boundary of the phase diagrams were characterized by slower kinetics, while samples that are deeper inside the phase diagrams exhibited faster kinetics (Figure 3D,E). For the latter condition, all polymer-rich droplets nucleated in the mixing region within milliseconds, and in the heating zone we could only monitor growth and coarsening events (Figure 3C). The observed timescale of milliseconds is consistent with a non-activated process dominated by diffusion. Moreover, our model predictions (Figure 2D) are qualitatively in well agreement with the experimental data (Figure 3D), and capture the slower kinetics of droplet formation with decreasing supersaturation.

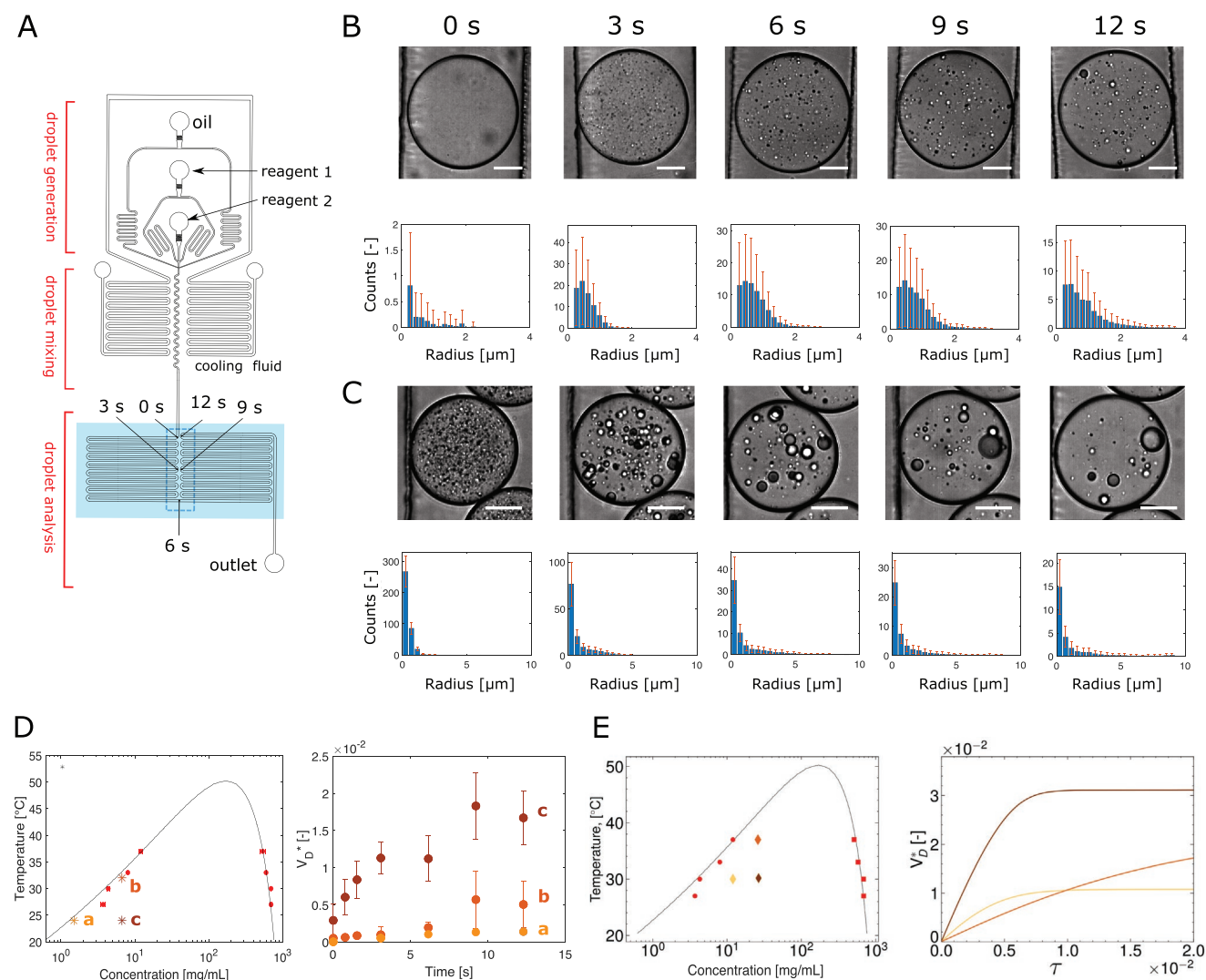


Figure 3. A) Schematic representation of the droplet microfluidic device to measure the kinetics of liquid–liquid phase separation over second timescales at different temperatures. Blue background indicates the heating zone; B–C) Representative brightfield image of an individual water-in-oil compartment in which LLPS is observed at different times in the middle of the channel. From image analysis we measured the size distribution of the droplets. Samples were B) 1.5 mg mL⁻¹ and C) 6.7 mg mL⁻¹ UCST-type polymer in 150 mM NaCl solution. Scale bars correspond to 30 μm. Dynamics of LLPS as a function of supersaturation. D) Time evolution of the total volume fraction of the dense phase (right panel) measured at different initial concentrations of the UCST polymer and different temperatures (indicated by labels a, b, and c in the phase diagram on the left). E) Prediction of the time evolution of the total volume fraction of the dense phase based on Equations (3)–(4) (right diagram) at different positions in the phase diagram indicated on the left.

5. Conclusion

We have leveraged droplet-based microfluidics to monitor liquid–liquid phase separation of polymer solutions in finite volumes comparable to cells. The heart of this strategy is the accurate measurement of the volume fraction of the dense polymer phase at different temperatures. Such measurements, which are challenging when using conventional bulk methods, open up the possibility of evaluating important thermodynamic and kinetic properties of liquid–liquid phase separation. Specifically, we measured the binodal lines determining the coexistence region of the two phases in a phase diagram in a label-free manner. In addition to thermodynamics, our measurements in finite volumes allowed estimation of the kinetic barrier of nucleation associated with the formation of a dense droplet in a parent dilute phase. Importantly, we can estimate the timescale of phase separation as a function of supersaturation even in case of a non-activated system dominated by diffusion. This strategy can now be used to evaluate the effect of different modulators (e.g., macromolecule sequence, crowding agents and buffer composition) on both the thermodynamics and the kinetics of liquid–liquid phase separation of polymer and protein solutions in cell-like volumes. These studies have significant implications for the design of materials with tailored properties and stimulus responsiveness.^[37]

Supporting Information

Supporting Information is available from the Wiley Online Library or from the author.

Acknowledgements

The authors thank Matteo Pirson, Charlotte Seiffert and Florence Stoffel (ETH Zurich) for help with experiments, and Dr. J. C. Thiele (University of Göttingen) for technical discussions. They gratefully acknowledge the Swiss National Science Foundation (Grant No. 205321_17905), the Synapsis Foundation for Alzheimer's disease (Zurich), and the European Research Council through the Horizon 2020 research and innovation programme (grant agreement No. 101002094) for financial support. L.L. and M.S. thank the Leverhulme Trust for funding under the project RPG-2019-235.

Open access funding provided by Eidgenössische Technische Hochschule Zurich.

Conflict of Interest

The authors declare no conflict of interest.

Author Contributions

P.A., M.S., S.S., and A.d.M. designed the study; A.V., S.S. and A.d.M. designed the microfluidic devices; M.S. designed the nucleation model; A.V., U.C.P., P.M., and G.P. performed experiments, A.V., T.S., L.L., and M.S. analyzed the data and developed the model; P.A. and U.C.P. wrote the initial draft; all authors edited and commented the manuscript; P.A., M.S., and A.d.M. acquired funding.

Data Availability Statement

The data that support the findings of this study are available from the corresponding author upon reasonable request.

Keywords

complete phase diagrams, finite volumes, kinetics, liquid–liquid phase separation, microfluidics, polymers and proteins, thermodynamics

Received: April 26, 2022

Revised: August 25, 2022

Published online: September 30, 2022

- [1] M. Sponchioni, U. Capasso Palmiero, D. Moscatelli, *Mater. Sci. Eng., C* **2019**, 102, 589.
- [2] C. E. Sing, S. L. Perry, *Soft Matter* **2020**, 16, 2885.
- [3] R. A. Kapelner, V. Yeong, A. C. Obermeyer, *Curr. Opin. Colloid Interface Sci.* **2021**, 52, 101407.
- [4] T. Lu, K. K. Nakashima, E. Spruijt, *J. Phys. Chem. B* **2021**, 125, 3080.
- [5] A. A. Hyman, C. A. Weber, F. Jülicher, *Annu. Rev. Cell Dev. Biol.* **2014**, 30, 39.
- [6] N. A. Yewdall, A. A. M. André, T. Lu, E. Spruijt, *Curr. Opin. Colloid Interface Sci.* **2021**, 52, 101416.
- [7] R. R. Poudyal, R. M. Guth-Metzler, A. J. Veenis, E. A. Frankel, C. D. Keating, P. C. Bevilacqua, *Nat. Commun.* **2019**, 10, 490.
- [8] B. Ghosh, R. Bose, T. Y. D. Tang, *Curr. Opin. Colloid Interface Sci.* **2021**, 52, 101415.
- [9] H. M. Fares, A. E. Marras, J. M. Ting, M. V. Tirrell, C. D. Keating, *Nat. Commun.* **2020**, 11, 5423.
- [10] M. Abbas, W. P. Lipiński, K. K. Nakashima, W. T. S. Huck, E. Spruijt, *Nat. Chem.* **2021**, 13, 1046.
- [11] B. G. O'Flynn, T. Mittag, *Curr. Opin. Cell Biol.* **2021**, 69, 70.
- [12] C. D. Crowe, C. D. Keating, *Interface Focus* **2018**, 8:20180032.
- [13] K. M. Ruff, F. Dar, R. V. Pappu, *Proc. Natl. Acad. Sci. USA* **2021**, 118, e2017184118.
- [14] E. W. Martin, J. B. Hopkins, T. Mittag, *Methods Enzymol.* **2021**, 646, 185.
- [15] M. Linsenmeier, M. R. G. Kopp, S. Stavrakis, A. De Mello, P. Arosio, *Biochim. Biophys. Acta, Mol. Cell Res.* **2021**, 1868, 118823.
- [16] P. Li, X. Zeng, S. Li, X. Xiang, P. Chen, Y. Li, B.-F. Liu, *Anal. Chem.* **2022**, 94, 687.
- [17] M. R. G. Kopp, M. Linsenmeier, B. Hettich, S. Prantl, S. Stavrakis, J. Leroux, P. Arosio, *Anal. Chem.* **2020**, 92, 5803.
- [18] E. Sokolova, E. Spruijt, M. M. K. Hansen, E. Dubuc, J. Groen, V. Chokkalingam, A. Piruska, H. A. Heus, W. T. S. Huck, *Proc. Natl. Acad. Sci. U. S. A.* **2013**, 110, 11692.
- [19] J. Shim, G. Cristobal, D. R. Link, T. Thorsen, Y. Jia, K. Piattelli, S. Fraden, *JACS* **2007**, 129, 8825.
- [20] A. Bremer, T. Mittag, M. Heymann, *Lab Chip* **2020**, 20, 4225.
- [21] W. E. Arter, R. Qi, G. Krainer, T. J. Welsh, Y. Xu, P. S. George-Hyslop, S. Alberti, T. P. J. Knowles, *bioRxiv* **2020**, <https://doi.org/10.1101/2020.06.04.132308>.
- [22] E. G. P. Stender, S. Ray, R. K. Norrild, J. A. Larsen, D. Petersen, A. Farzadfar, C. Galvagnion, H. Jensen, A. K. Buell, *Nat. Commun.* **2021**, 12, 7289.
- [23] J. A. Thomson, P. Schurtenberger, G. M. Thurston, G. B. Benedek, *Proc. Natl. Acad. Sci. USA* **1987**, 84, 7079.
- [24] M. L. Broide, C. R. Berland, J. Pande, O. Ogun, G. B. Benedek, *Proc. Natl. Acad. Sci. U. S. A.* **1991**, 88, 5660.
- [25] F. Cardinaux, T. Gibaud, A. Stradner, P. Schurtenberger, *Phys. Rev. Lett.* **2007**, 99, 118301.
- [26] M. Muschol, F. Rosenberger, *J. Chem. Phys.* **1997**, 107, 1953.

- [27] S. D. Vela, M. K. Braun, A. Do, A. Greco, J. Mo, Z. Fu, F. Zhang, F. Schreiber, *Soft Matter* **2016**, 12, 9334.
- [28] M. T. Wei, S. Elbaum-Garfinkle, A. S. Holehouse, C. C. H. Chen, M. Feric, C. B. Arnold, R. D. Priestley, R. V. Pappu, C. P. Brangwynne, *Nat. Chem.* **2017**, 9, 1118.
- [29] S. F. Banani, H. O. Lee, A. A. Hyman, M. K. Rosen, *Nat. Rev. Mol. Cell Biol.* **2017**, 18, 285.
- [30] T. J. Nott, E. Petsalaki, J. D. Forman-kay, A. J. Baldwin, T. J. Nott, E. Petsalaki, P. Farber, D. Jervis, E. Fussner, A. Plochowitz, T. D. Craggs, D. P. Bazett-jones, T. Pawson, J. D. Forman-kay, A. J. Baldwin, *Mol. Cell* **2015**, 57, 936.
- [31] J. P. Brady, P. J. Farber, A. Sekhar, Y. Lin, R. Huang, A. Bah, T. J. Nott, H. S. Chan, A. J. Baldwin, J. D. Forman-Kay, L. E. Kay, *Proc. Natl. Acad. Sci. U. S. A.* **2017**, 114, E8194.
- [32] E. W. Martin, A. S. Holehouse, I. Peran, M. Farag, J. J. Incicco, A. Bremer, C. R. Grace, A. Soranno, R. V. Pappu, T. Mittag, *Science* **2020**, 367, 694.
- [33] A. Bremer, M. Farag, W. M. Borchers, I. Peran, E. W. Martin, R. V. Pappu, T. Mittag, *Nat. Chem.* **2021**, 14, 196.
- [34] A. M. Küffner, M. Prodan, R. Zuccarini, U. C. Palmiero, L. Faltova, P. Arosio, *ChemSystemsChem* **2020**, 2, e2000001.
- [35] P. M. McCall, K. Kim, A. W. Fritsch, J. M. Iglesias-Artola, L. M. Jawerth, J. Wang, M. Ruer, J. Peychl, A. Poznyakovskiy, J. Guck, S. Alberti, A. A. Hyman, J. Brugués, *bioRxiv*, **2020**, <https://doi.org/10.1101/2020.10.25.352823>.
- [36] M. Linsenmeier, M. R. G. Kopp, F. Grigolato, L. Emmanoulidis, D. Liu, Z. Dominik, M. Hondele, K. Weis, U. C. Palmiero, P. Arosio, *Angew. Chem., Int. Ed.* **2019**, 58, 14489.
- [37] U. Capasso Palmiero, C. Paganini, M. R. G. Kopp, M. Linsenmeier, A. M. Küffner, P. Arosio, *Adv. Mater.* **2021**, 34, 2104837.
- [38] A. Molliex, J. Temirov, J. Lee, M. Coughlin, A. P. Kanagaraj, H. J. Kim, T. Mittag, J. P. Taylor, *Cell* **2015**, 163, 123.
- [39] E. W. Martin, T. Mittag, *Biochemistry* **2018**, 57, 2478.
- [40] D. E. Meyer, A. Chilkoti, *Biomacromolecules* **2004**, 5, 846.
- [41] N. K. Li, F. G. Quiroz, C. K. Hall, A. Chilkoti, Y. G. Yingling, *Biomacromolecules* **2014**, 15, 3522.
- [42] L. Faltova, A. M. Küffner, M. Hondele, K. Weis, P. Arosio, *ACS Nano* **2018**, 12, 9991.
- [43] X. Cao, Y. Du, A. Küffner, J. Van Wyk, P. Arosio, J. Wang, P. Fischer, S. Stavarakis, A. DeMello, *Small* **2020**, 16, 1907534.
- [44] H. Song, R. F. Ismagilov, *J. Am. Chem. Soc.* **2003**, 125, 14613.
- [45] A. Huebner, D. Bratton, G. Whyte, M. Yang, J. Andrew, F. Hollfelder, *Lab Chip* **2009**, 9, 692.
- [46] S. F. Shimobayashi, P. Ronceray, D. W. Sanders, M. P. Haataja, C. P. Brangwynne, *Nature* **2021**, 599, 503.
- [47] A. Narayanan, A. Meriin, J. O. Andrews, J. Spille, M. Y. Sherman, I. I. Cisse, *eLife* **2019**, 8, e39695.
- [48] A. E. Posey, K. M. Ruff, J. M. Lalmansingh, T. S. Kandola, J. J. Lange, R. Halfmann, R. V. Pappu, *J. Mol. Biol.* **2021**, 433, 166848.
- [49] E. W. Martin, T. S. Harmon, J. B. Hopkins, S. Chakravarthy, J. J. Incicco, P. Schuck, A. Soranno, T. Mittag, *Nat. Commun.* **2021**, 12, 4513.
- [50] D. Reguera, R. K. Bowles, Y. Djikaev, H. Reiss, *J. Chem. Phys.* **2003**, 118, 340.
- [51] R. Grossier, S. Veessler, *Cryst. Growth Des.* **2009**, 9, 1917.
- [52] M. Salvalaglio, C. Perego, F. Giberti, M. Mazzotti, M. Parrinello, *Proc. Natl. Acad. Sci. U. S. A.* **2015**, 112, E6.
- [53] Y. S. Jho, H. Y. Yoo, Y. Lin, S. Han, D. S. Hwang, *Adv. Colloid Interface Sci.* **2017**, 239, 61.
- [54] J. Wedekind, D. Reguera, *J. Phys. Chem. B* **2008**, 112, 11060.
- [55] B. C. Knott, V. Molinero, M. F. Doherty, B. Peters, *J. Am. Chem. Soc.* **2012**, 134, 19544.